Optics Letters

Single-shot local measurement of terahertz correlated second harmonic generation in laser air plasma filaments

Mervin Lim Pac Chong,[1,†] Kareem J. Garriga Francis,[2,†] E. Yiwen,[2] and Xi-Cheng Zhang[1,2,*]

[1] Laboratory for Laser Energetics, University of Rochester, Rochester, New York 14623, USA
[2] The Institute of Optics, University of Rochester, Rochester, New York 14627, USA
[†] These authors contributed equally to this work.
*xi-cheng.zhang@rochester.edu

Received 23 October 2023; revised 9 December 2023; accepted 11 December 2023; posted 11 December 2023; published 1 January 2024

We present a single-shot detection method of terahertz correlated second harmonic generation in plasma-based sources by directly mixing an optical probe into femtosecond laser-induced plasma filaments in air. The single-shot second harmonic trace is obtained by measuring a second harmonic generation on a conventional CCD with a spatiotemporally distorted probe beam. The system shows a spectrometer resolution of 22 fs/pixel on the CCD and a true resolution on the order of the probe pulse duration. With considerable THz peak electric field strength, this formalism can open the door to single-shot THz detection without bandwidth limitations.
© 2024 Optica Publishing Group

https://doi.org/10.1364/OL.510070

In recent years, the development of large-scale laser facilities has led to major contributions in terahertz (THz) and plasma sciences. Recently, >1 J lasers showcased a record-setting optical-to-THz energy conversion in lithium niobate exceeding 1.2% [1]. Similar facilities were also used to produce large THz peak electric field strengths above MV/cm in plasma [2]. The traditional method to fully characterize the THz emission from sources has been through electro-optic sampling (EOS) [3–6]; but, with increasing THz electric field strength, electro-optic (EO) crystal over-rotation poses an issue in accurately representing a signal with minimal distortion. The crystal structure also limits the spectral detection bandwidth.

Terahertz Field-Induced Second Harmonic (TFISH) generation offers a platform for broad spectral detection range. It mixes optical photons with THz photons in a third-order nonlinear process to produce a second harmonic (SH) of the fundamental optical photons [7]. The TFISH signal can also be mixed with a reference SH signal to yield a coherent signal through homodyne detection.

In this Letter, a potential method for a single-shot detection of a broadband THz pulse is presented by directly mixing an optical probe onto a two-color femtosecond laser-induced air plasma. We designed a noncollinear TFISH generation by mixing a probe beam onto the plasma at 40° incidence with respect to the pump propagation axis. In previous results, we showed that the system provides an SH signal that is correlated to the THz field through the TFISH model [8,9], and the temporal and polarization dynamics were studied in Ref. [10]. Despite other interpretations of SH in plasma [11–14], the temporally gated signals found in this study and the high conversion efficiency are new. It is currently not definitive that the appearance of the strong SH is explicitly field induced in the traditional sense. Since many linear and nonlinear processes occur in the creation of a plasma filament, theoretical analysis of the system is complicated. Work to determine the authenticity of the signals as THz field induced or a consequence of the same physics is ongoing. We continue to use TFISH in this paper to easily present the data.

As shown in Fig. 1, the noncollinear TFISH system consists of a two-color air plasma THz source where the probe beam intersects the plasma at 40° incidence. A Coherent Astrella amplified laser system operating at 6.5 W, 1 kHz repetition rate, and near 100 fs is used. The laser fundamental wavelength is 800 nm (ω) with a 12 mm at $1/e^2$ initial beam spot size. The pump and probe paths are 5.2 and 1.3 W, respectively. A 100 μm-thick type I β-Barium Borate (BBO 1) crystal is placed after the 300 mm pump lens (L1) to maximize the THz field strength.

An 800 lp/mm grating is used to produce a 40° pulse-front tilt (PFT) along the intensity-front of the probe with respect to its wavefront [15], and thus encode temporal information onto spatial coordinates. This configuration is hereby referred to as a single-shot/real-time PFT system. The PFT is imaged from the grating to the lens L1's focal region with a Keplerian telescope consisting of a pair of cylindrical lenses with focal lengths 300 mm (L2) and 100 mm (L3). This is considered the "grating-imaging system." Since the PFT probe is effectively collimated in the interaction region between the probe and the plasma, a third cylindrical 200 mm lens (L4) is used to focus the beam orthogonally (vertical axis) to the induced PFT. The result is a higher intensity along a line in the focal region. The interaction is imaged to a CCD by a Keplerian telescope using spherical lenses. Filters and dichroic mirrors are used to discriminate the TFISH signal from the fundamental probe.

To achieve coherent detection, a second 100 μm-thick type I β-Barium Borate, labeled as BBO 2 in Fig. 1, is used in the probe beam path to produce a reference wave. When the polarization of

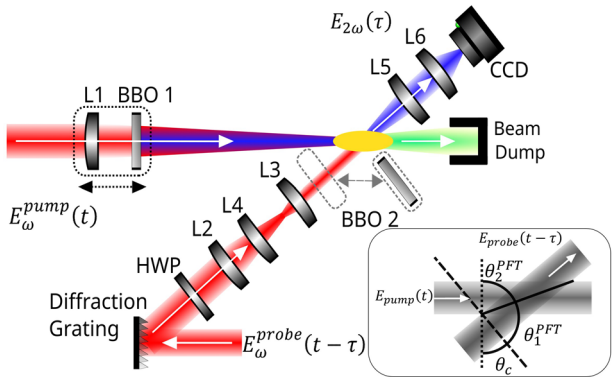

Fig. 1. Experimental setup. The pulse-front tilt (PFT) is imaged onto the interaction region by a Keplerian telescope. A CCD detects the SH generated, which is isolated with a dichroic mirror (Thorlabs DMLP490 L) and two bandpass filters (Thorlabs FBH400-40). BBO 1 and BBO 2 are β-BBO crystals. L1–L6 are lenses. HWP is a half-wave plate. The inset shows the angles at the interaction region: θ_C is the pump-probe angle, and θ_i^{PFT} is the PFT angle where i is 1 or 2. The dashed and dotted lines are the phase fronts of the probe and pump beams, respectively, and the solid line represents the probe PFT.

the SH wave induced by BBO 2 has components along the same axis as the polarization of the TFISH signal, an interferometric process leads to a coherent homodyne detection of the THz field. Hence, a half-wave plate (HWP) and the BBO 2 orientation are used to adjust the former. A delay line in the probe beam path aids in the spatiotemporal overlap.

The multi-shot behavior of the noncollinear system and the TFISH signals retrieved at the pump–probe spatiotemporal overlap have been shown in Refs. [8,9]. Due to the nature of a plasma-filament, there exists a localized TFISH signal maxima because of the varying electron number density along the propagation axis, which is found by moving L1 and BBO 1 together through the probe beam focus [8,9].

The noncollinear system can be modeled using the TFISH process to retrieve a signal:

$$S_{2\omega} \propto \int_{-\infty}^{\infty} \left|\chi^{(3)}(2\omega)\, E_{\omega}^{2}\,(t - \tau - \alpha_{PFT}x)\, E_{THz}^{*}(t)\right|^{2} \partial t, \quad \textbf{(1)}$$

where $S_{2\omega}$ is the signal detected by the PMT, $\chi^{(3)}(2\omega)$ is the third-order susceptibility tensor of air within the plasma, $E_{\omega}(t \pm \tau - \alpha_{PFT}x)$ is the electric field of the probe beam delayed by a temporal factor τ and influenced by PFT with α_{PFT} in s/m, x is the transverse coordinate, and $E_{THz}(t)$ is the THz field confined to the plasma filament. The probe beam is incident onto the grating at 0° leading to an initial diffraction at 40°. The PFT at the grating is directly imaged to the interaction region. The linear propagation from the grating to the CCD is modeled using Kostenbauder matrices [16,17] (K-matrices), yielding a total induced PFT angle of 70° at the interaction region with the following 4 × 4 K-matrix:

$$K_{\text{int}} = \begin{bmatrix} \frac{f_3}{f_2\sigma} & 0 & 0 & 0 \\ 0 & \frac{f_2\sigma}{f_3} & 0 & -\frac{f_2\lambda\xi}{f_3 c} \\ -\frac{\xi}{c\sigma} & 0 & 1 & 0 \\ 0 & 0 & 0 & 1 \end{bmatrix} = \begin{bmatrix} A & B & 0 & E \\ C & D & 0 & F \\ G & H & 1 & I \\ 0 & 0 & 0 & 1 \end{bmatrix},$$

where f_2 and f_3 are the focal lengths of L_2 and L_3, respectively, σ is the angular grating magnification, λ is the probe beam fundamental center wavelength, ξ is the grating angular dispersion parameter, and c is the speed of light in air [18]. Note that L4 is omitted since it has no effect in the angle of the PFT. Parameters A, B, C, and D of the K-matrix form the well-known ABCD matrix, with a temporal counterpart in the bottom right quadrant with parameter I being the group delay dispersion. The spatiotemporally coupled terms E, F, G, and H denote the spatial chirp, angular dispersion, PFT, and time versus angle, respectively [16,17]. A spatiotemporal Gaussian pulse yields a reduced Q-Matrix at the interaction region given by [17]

$$Q = \frac{\begin{bmatrix} A & 0 \\ G & 1 \end{bmatrix} \cdot Q_{in} + \begin{bmatrix} B & \frac{E}{\lambda} \\ H & \frac{I}{\lambda} \end{bmatrix}}{\begin{bmatrix} C & 0 \\ 0 & 0 \end{bmatrix} \cdot Q_{in} + \begin{bmatrix} D & \frac{F}{\lambda} \\ 0 & 1 \end{bmatrix}} = j\frac{\lambda}{\pi}\begin{bmatrix} Q_{xx} & Q_{xt} \\ -Q_{xt} & Q_{tt} \end{bmatrix}^{-1}.$$

The output field becomes $E(x,z,t) = e^{[x^2 Q_{xx} + 2xtQ_{xt} - t^2 Q_{tt}]}$, where Q_{xx} describes the spatial Gaussian parameters, Q_{xt} is the coupling term, and Q_{tt} describes the temporal width of the pulse. The input Q-matrix Q_{in} (before the grating) describes the initial probe, with $Q_{xt} = 0$. The PFT is extracted from Q by $\alpha_{PFT} = \frac{\Re\{Q_{xt}\}}{\Re\{Q_{tt}\}}$ and described by the angle $\theta_{PFT} = tan^{-1}(\alpha_{PFT}c)$ between the beam's intensity front and wavefront [15]. The extension of the K- and Q-matrices to the CCD plane from the grating plane is simulated and carried out in MATLAB.

The noncollinear geometry leads to an effective PFT angle $\theta_2^{PFT} = 180° - \theta_1^{PFT} - \theta_C$, where θ_2^{PFT} is the PFT angle in the interaction region, θ_1^{PFT} is the PFT angle imaged with the first telescope, and θ_C is the angle between the pump and the probe. In the interaction region, the beam is an ellipse with horizontal and vertical waist radii of 1 mm and 9 μm, respectively. A careful alignment is vital for the minimum TFISH trace size during the spatiotemporal overlap.

Figure 2 shows the simulations of the PFT system using a K-matrix solver from the grating to the CCD for initial probe beam diameters D_{in} = 5, 12, and 20 mm. The simulation accounts

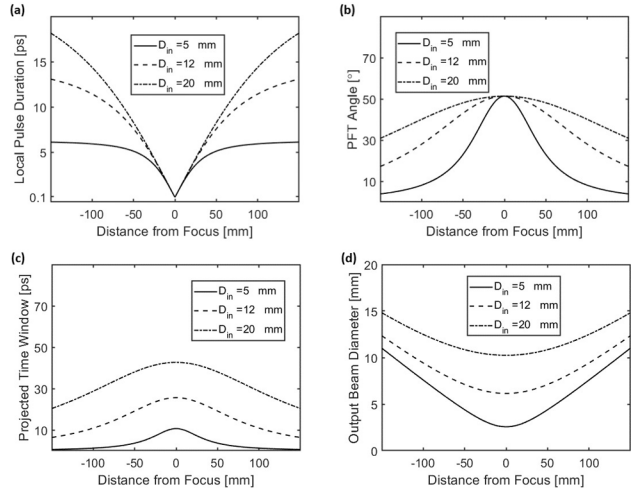

Fig. 2. Simulation results of a K-matrix solver for system optimization using three initial probe beam diameters. (a) Beam pulse duration lengthening due to the angular dispersion as a function of distance from the CCD (lens focal plane). (b) Maximum achievable PFT versus distance from the CCD. (c) Maximum achievable time window versus distance from CCD. (d) Output beam diameter versus distance from the CCD.

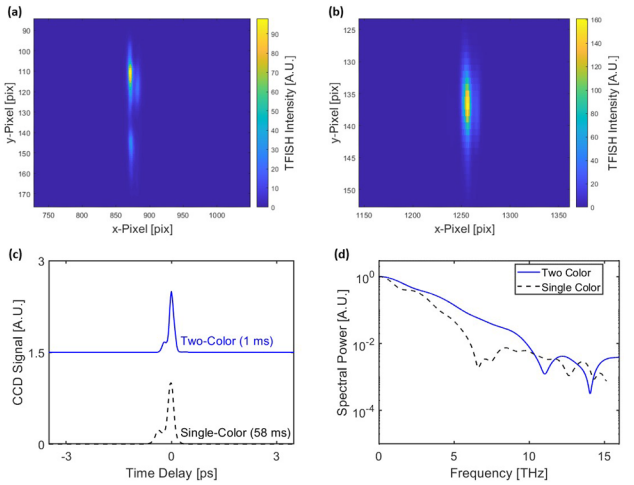

Fig. 3. Real-time detection results. (a) and (b) are the real-time SH image gathered at the CCD for single- and two-color pumped signals, respectively. (c) Temporal TFISH signal for two-color (solid line) and single-color (dashed line) pumps resulting from integrating over the row (y-) pixels. The waveforms are flipped along the temporal axis to match previous results and vertically shifted for clarity. (d) Spectra corresponding to the TFISH signals.

for the doubled PFT magnification by the Keplerian telescope after the interaction region. Although the PFT angle reduces from 70° to 50°, the setup becomes physically easier. From Fig. 2(a), the grating image plane is the only point where the probe pulse-duration is preserved, and the spatiotemporal overlap is undistorted—yielding the maximum possible PFT angle for a given system as shown in Fig. 2(b). Moving away from the focus leads to a larger pulse duration and thus, loss of information according to Eq. (1). In Fig. 2(c), as the initial diameter is increased, the tolerance in localizing the maximum PFT angle and the time window are relaxed at the tradeoff of the pulse duration as seen in Fig. 2(a). This is due to the elimination of the spatial chirp and group delay dispersion at the overlapping point, which has a 0.6 mm theoretical tolerance for an 800 lines/mm grating.

Figure 2(d) shows that as the beam diameter onto the grating is increased, the divergence from the angular dispersion is relaxed. In our experiment, a 12 mm diameter beam was chosen because it yielded good experimental tolerances without needing large aperture optics.

The overlapped spatial region directly yields a temporal coordinate through expressions [6] $T_W = \frac{D tan\theta_2^{PFT}}{c}$ and $\Delta t_R = \frac{\Delta x tan\theta_2^{PFT}}{c}$, representing the temporal window and device-limited resolution, respectively. Here, T_W represents the spatiotemporally coupled total detection time window, D is the optical beam diameter, Δt_R is the temporal resolution per CCD pixel, and Δx is the CCD pixel width. When the interaction region is directly imaged to the CCD, a y-pixel integration leads to the temporal detection of the TFISH signal due to the linear relationship between T_W and D.

In Fig. 3(a), the real-time trace of the TFISH signal for a single-color excitation pump plasma is achieved by omitting BBO 1. Because the single-color signal is weak, a higher probe pulse energy (1.2 mJ at 1 kHz) and a longer exposure time (60 ms) on the CCD are required to produce a visible trace. The result remains a real-time trace where no delay scan is needed and can be done in single-shot with a 9.3 mJ pulse energy. Decreasing the probe beam diameter for a lower single-shot energy operation will incur a cost on the time window. Furthermore, increasing intensity and the trace visibility by reducing L3 inherently increases the PFT angle, lowering the temporal resolution. In Fig. 3(b), because the TFISH trace shown is for a two-color pump plasma, even a <130 μJ optical probe beam energy yields good visibility at an exposure time of 1 ms. This signal is effectively single-shot and theoretically requires no average.

To retrieve the temporal trace, we average over every row of pixels. The traces for a single-color and two-color sources are shown in Fig. 3(c) at an exposure of 58 and 1 ms, respectively, and their corresponding power spectrum is shown in Fig. 3(d). The two-color trace is easily visible to the human eye. Figure 3 is background-free because the process, according to Eq. (1), is inherently so. Other secondary SH radiation processes may still lead to the appearance of DC components in Fig. 3(d).

The CCD used in the experiment (Imaging Source DMK 27BUP031) has a 2.2 μm pixel size. Experimentally, the PFT method shows a resolution of 22 fs/pix and is measured by the time difference ratio over the number of pixels the peak of a signal shifted between two different time delay positions. This spectrometer resolution is different from the real resolution. The latter is found through the convolution between the probe optical pulse and Gaussian spectrometer function with a width set to 22 fs, resulting in a resolution near the probe pulse duration. Since the PFT method encodes the temporal information directly onto the spatial width of the probe beam, a very large time window is accessible. In Fig. 3(c), despite the maximum achievable time window is within the theoretical expectation of 15 ps, the THz beam size limits it to 1 ps. While relatively short, this method can still be expanded to systems with a larger THz beam diameter. For example, a 15 ps time window is possible with only a 2 mm diameter focused THz beam.

The coherent signal for the two-color source is found through the interferometric mixing of the TFISH signal with a controlled SH. Using the BBO 2 crystal, the 2ω (400 nm) probe is termed a Local Field-Induced Second Harmonic (LFISH) generated wave. Considering that some of the ω probe beam propagates unconverted, the interferometric mixing of the two SH signals takes the form:

$$S_{2\omega} \propto \left|E_{2\omega}^{LFISH} + E_{2\omega}^{TFISH}\right|^2. \quad (2)$$

The above expression produces two incoherent intensity traces and a cross-correlated term known as the Optically Biased Coherent Detection (OBCD) term [19]. A background subtraction operation is required to extract the OBCD term. The OBCD trace for a two-color source is shown in Fig. 4(a) along with its Fourier transform in Fig. 4(b). In this case, probe instabilities clearly outline the time window as limited by the width of the THz beam (since it is smaller than the horizontal width of the probe). The PFT coherent detection is done with a 1 ms exposure time, making it effectively single-shot for our 1 kHz repetition rate laser pulses.

The THz spectrum can still be limited by alignment constraints. The BBO 2 crystal has a small aperture and part of the PFT trace, and thus the probe spectrum, is clipped as it must be placed in a region of dominant spatial chirp to avoid crystal damage. When the PFT is established at the interaction region, the clipped trace results in an artificial lengthening of the probe pulse from the time–bandwidth product. Because the

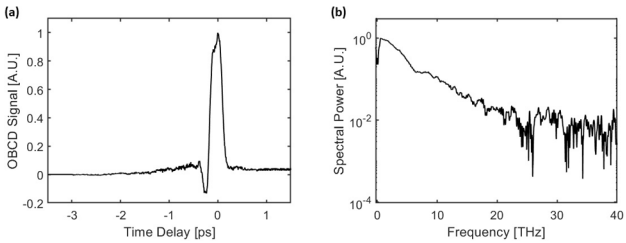

Fig. 4. (a) Single-shot OBCD signal from the PFT configuration gathered at 1 ms exposure time. (b) Corresponding spectral power of (a) obtained through mathematical Fourier transform.

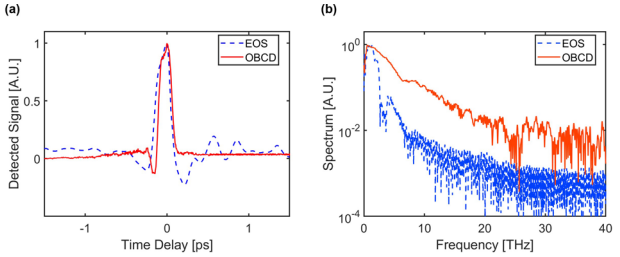

Fig. 5. Comparison of a plasma source characterized by a single-shot EOS (blue) and a single-shot OBCD (red) in (a) time, and (b) their respective frequency spectra.

beam is spatiotemporally coupled, the signal becomes slightly distorted, and the maximum detection spectrum decreases proportionally to the increase in the probe pulse duration. Before the interaction region, the temporal information is not yet localized along the probe beam, and from an angular dispersion, clipping the edges of the beam can lead to reduced information in the overall signal. Yet, the recovered spectrum still boasts detection capabilities beyond what is possible with a single-shot EOS.

For completeness, the single-shot OBCD signal is further compared with a PFT-based single-shot EOS signal from setups like Refs. [20,21] in Fig. 5. In our case, the PFT for the single-shot EOS is induced with a 1200 lp/mm grating and the detection crystal is a 1 mm thick ZnTe. The same pump–probe angle, plasma source, and CCD are used in both cases. The temporal lineouts are compared in Fig. 5(a), and their respective frequency spectra are compared in Fig. 5(b). Both systems have a similar signal-to-noise ratio of ∼200 and dynamic range of ∼103. They differ in bandwidth and probe energy required. OBCD sees a tenfold improvement in detection bandwidth (>20 THz) compared to EOS (2.5 THz). EOS, expectedly, requires <10 nJ of probe energy, whereas OBCD requires <130 μJ. Since the probe energy required for OBCD is still very low, it remains a better option, especially for higher spectral components analysis.

In summary, we present the local measurement of the THz intensity profile and the electric field profile inside the plasma by mixing a spatiotemporally coupled probe beam directly into the plasma. The high visibility resulting trace serves as a powerful diagnostic of THz radiation in plasma-based sources. A broad detection bandwidth is recovered for a two-color air–plasma THz source. Since a single-shot EOS concept works here, the detection window and the resolution can be improved with other spatiotemporal couplings. An angular dispersion without PFT can yield a high resolution and a high temporal window characterization of THz waves.

Funding. National Science Foundation (ECCS-2152081); Air Force Office of Scientific Research (FA9550-21-1-0300, FA9550-21-1-0389); National Nuclear Security Administration (DE-NA003856).

Acknowledgment. The authors would like to thank Shing Yiu Fu, Jiacheng Zhao, and Zhigong Gao for their help that led up to this work. This material is based upon work supported by the Department of Energy National Nuclear Security Administration under Award Number DE-NA003856, the University of Rochester, and the New York Energy Research and Development Authority. This report was prepared as an account of work sponsored by an agency of the U.S. Government. Neither the U.S. Government nor any agency thereof, nor any of their employees, makes any warranty, express or implied, or assumes any legal liability or responsibility for the accuracy, completeness, or usefulness of any information, apparatus, product, or process disclosed, or represents that its use would not infringe privately owned rights. Reference herein to any specific commercial product, process, or service by trade name, trademark, manufacturer, or otherwise does not necessarily constitute or imply its endorsement, recommendation, or favoring by the U.S. Government or any agency thereof. The views and opinions of authors expressed herein do not necessarily state or reflect those of the U.S. Government or any agency thereof.

Disclosures. The authors declare no conflicts of interest.

Data availability. Data underlying the results presented in this paper are not publicly available at this time but may be obtained from the authors upon reasonable request.

REFERENCES

1. X. Wu, D. Kong, S. Hao, *et al.*, in *47th International Conference on Infrared, Millimeter and Terahertz Waves* (2022), p. 1.
2. A. D. Koulouklidis, C. Gollner, V. Shumakova, *et al.*, Nat. Commun. **11**, 292 (2020).
3. Q. Wu and X.-C. Zhang, Appl. Phys. Lett. **67**, 3523 (1995).
4. Z. Jiang and X.-C. Zhang, Appl. Phys. Lett. **72**, 1945 (1998).
5. G. Sharma, K. Singh, I. Al-Naib, *et al.*, Opt. Lett. **37**, 4338 (2012).
6. S. M. Teo, B. K. Ofori-Okai, C. A. Werley, *et al.*, Rev. Sci. Instrum. **86**, 051301 (2015).
7. J. Dai, X. Xie, and X.-C. Zhang, Phys. Rev. Lett. **97**, 103903 (2006).
8. K. Garriga Francis, M. Lim Pac Chong, E. Yiwen, *et al.*, Opt. Lett. **47**, 6297 (2022).
9. K. J. Garriga Francis and X.-C. Zhang, Front. Optoelecton. **16**, 44 (2023).
10. S. Y. Fu, K. J. Garriga Francis, M. Lim Pac Chong, *et al.*, Opt. Lett. **48**, 3199 (2023).
11. D. S. Bethune, Phys. Rev. A **23**, 3139 (1981).
12. Y. D. Qin, H. Yang, C. J. Zhu, *et al.*, Appl. Phys. B: Lasers Opt. **71**, 581 (2000).
13. M. Beresna, P. G. Kazansky, Y. Svirko, *et al.*, Appl. Phys. Lett. **95**, 121502 (2009).
14. G. Li, J. Ni, H. Xie, *et al.*, Opt. Lett. **39**, 961 (2014).
15. J. Hebling, Opt. Quantum Electron. **28**, 1759 (1996).
16. A. G. Kostenbauder, IEEE J. Quantum Electron. **26**, 1148 (1990).
17. S. Akturk, X. Gu, P. Gabolde, *et al.*, Opt. Express **13**, 8642 (2005).
18. M. A. Vieira Fernandes, "Analysis of spatio-temporal distortions in chirped pulse amplification lasers," Universidade Técnica de Lisboa (2009).
19. C.-Y. Li, D. V. Seletskiy, Z. Yang, *et al.*, Opt. Express **23**, 11436 (2015).
20. Z.-H. Zhai, S.-C. Zhong, J. Li, *et al.*, Rev. Sci. Instrum. **87**, 095101 (2016).
21. J. Shan, A. S. Weling, E. Knoesel, *et al.*, Opt. Lett. **25**, 426 (2000).

128.151.33.245 on 2024-09-01 17:14:21